A Systematic Approach to Design Amplitude Estimators for NTD-PLL: Performance Improvement Under Abnormal Grid Disturbances

Mohd. Afroz Akhtar, *Member, IEEE*, Suman Saha, Dibyendu Pal, Anant Kumar Verma, *Member, IEEE*, and Zoheir Tir, *Senior Member, IEEE*

***Abstract*—Nonfrequency-dependent transport delay-phase-locked loop (NTD-PLL) is one of the simple grid synchronization approaches that aims to improve the phase and frequency estimation under frequency deviation. However, its amplitude estimation still exhibits double-frequency oscillations that are larger in magnitude as compared to the conventional transport delay (TD)-PLL counterpart. To overcome this challenge, two systematic approaches to design amplitude estimators (AEs) for NTD-PLL are presented in this article. One approach includes eliminating double-frequency oscillation error present in dq-frame component v_d, whereas another uses Pythagorean trigonometric identity in $\alpha\beta$-frame for accurate amplitude estimation. Due to the general form of AE proposed in $\alpha\beta$-frame, it can be easily applied in the design of other TD-based PLLs. The design aspects of these methods are discussed in detail, and the efficacy of the proposed structures is finally evaluated through numerical and experimental results. Some methods to enhance the performance of the AEs are explored and analyzed. This article provides useful insight to the designers regarding the advantages and disadvantages associated with the proposed AEs for their specific applications.**

***Index Terms*—Amplitude estimation, phase-locked loop (PLL), Pythagorean trigonometric identity (PTI), synchronization, transport-delay.**

I. Introduction

TRANSPORT delay based quadrature signal generator (TD-QSG), when configured as a TD-phase-locked loop (TD-PLL), as shown in Fig. 1, has been a widely used technique for synchronization of grid-connected inverters (GCIs) with the utility grid [1], [2], [3]. The TD-QSG utilizes fixed $T_s/4$ transport delay for creating a fictitious quadrature signal from a single input signal [4], [5], [6], where T_s is the time period of the fundamental component of the nominal grid frequency. It, however, suffers from offset errors and double-frequency oscillatory errors (DFOEs) in the estimated quantities, i.e., phase, frequency, and amplitude of the grid under frequency deviation [7], [8], [9].

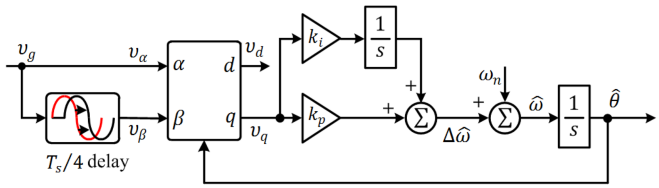

Fig. 1. Basic structure of the TD-PLL.

To overcome these issues, various state-of-the-art TD-PLLs have been proposed recently [1]. Among those, the enhanced TD-PLL (ETD-PLL) employs cascaded delayed signal cancellation (DSC) units to improve the harmonic filtering capability of TD-PLL [4]. However, it involves more TD units, mathematical operations as well as a phase compensator unit. Moreover, it is effective only when the frequency variations are small. An adaptive TD-PLL (ATD-PLL) is proposed in [10], which accurately generates the fictitious orthogonal signal under the frequency-varying environment using a fixed-length TD unit. Another technique called variable-length TD-PLL (VTD-PLL) is also suggested in [11] and [12] by adjusting the length of TD according to the grid frequency. However, these strategy demands a high computational effort [13] and the time-varying delay unit makes the small-signal modeling and the stability analysis rather difficult [12]. Introducing another $T_s/4$ delay in the transformation matrix (TM) to remove the offset errors in phase and frequency estimation during frequency drifts is proposed in [1], [4], and [14], the structure of which is called the nonfrequency-dependent TD-PLL (NTD-PLL). However, NTD-PLL only corrects the phase offset problem of basic TD-PLL during frequency jump, but cannot solve the DFOEs (refer to [4, Fig. 20] and [10, Fig. 11]). To mitigate this issue, cascading moving average filter and phase-lead compensator within the NTD-PLL loop is proposed in [14], though it increases the

Manuscript received 14 July 2022; revised 2 November 2022 and 27 November 2022; accepted 29 November 2022. Date of publication 2 December 2022; date of current version 14 February 2023. Recommended for publication by Associate Editor G. De Donato. *(Corresponding author: Mohd. Afroz Akhtar.)*

Mohd. Afroz Akhtar, Suman Saha, and Dibyendu Pal are with the Academy of Scientific and Innovative Research, Council of Scientific and Industrial Research–Central Mechanical Engineering Research Institute, Durgapur 713209, India, and also with the Aerosystems Laboratory, Council of Scientific and Industrial Research–Central Mechanical Engineering Research Institute, Durgapur 713209, India (e-mail: afrozakhtar@cmeri.res.in; s_saha@cmeri.res.in; dibyendu@cmeri.res.in).

Anant Kumar Verma is with the Electric Power Conversion System Laboratory, Universidad de O'Higgins, Rancagua 2820000, Chile (e-mail: anant.kumar@uoh.cl).

Zoheir Tir is with the LEVRES Laboratory, Faculty of Technology, University of El Oued, El-Oued 39000, Algeria (e-mail: tir-zoheir@univ-eloued.dz).

Color versions of one or more figures in this article are available at https://doi.org/10.1109/TPEL.2022.3226242.

Digital Object Identifier 10.1109/TPEL.2022.3226242

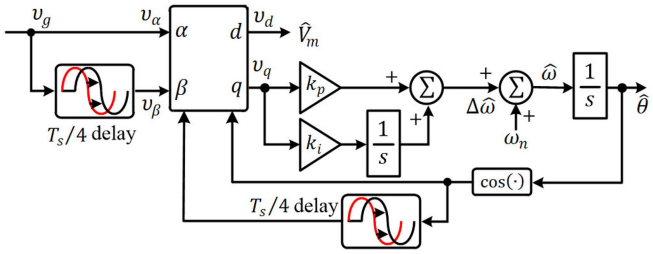

Fig. 2. Basic structure of the NTD-PLL. v_g is the grid voltage. Terms $\hat{V}_m$, $\hat{\omega}$, and $\hat{\theta}$ are the estimated amplitude, angular frequency, and phase angle of v_g, respectively. k_p and k_i are the control parameters.

order of the PLL structure, which rather complicates the design procedure. However, just by modifying the TM of NTD-PLL [15], [16], [17], the structure of which is shown in Fig. 2, eliminates the DFOEs present in phase and frequency estimations as well as the phase offset errors while inheriting the simplicity of the NTD-PLL, i.e., without changing the open-loop transfer function of the NTD-PLL. However, it will be discussed briefly in Sections II and III that it is susceptible to a larger magnitude of double-frequency oscillation in the amplitude estimation as compared to the TD-PLL during the frequency variations (refer to [17, Figs. 6(d) and 13(d)]).

In light of the above issues, an improved estimation of the amplitude of grid voltage using NTD-PLL under the frequency deviation is thus necessary. This article contributes to that by proposing two different double-frequency immune estimator (DFI-AE) strategies together with their detailed design procedures. The proposed strategies are capable of eliminating the DFOEs and enabling accurate estimation of grid voltage amplitude. One of the suggested DFI-AE strategies has a general form, therefore, it can also be applied to other TD-based PLLs with fixed-length TD units for amplitude estimation. In addition to this analysis, exploring some techniques and design guidelines to enhance the grid disturbance rejection capabilities of AEs is another aim of this article. The efficacies of the suggested AEs are finally validated against well-known PLLs using numerical and experimental results.

II. NTD-PLL and DFOEs in Amplitude Estimation

In this section, a brief overview of NTD-PLL is presented. Also, the linear time-invariant (LTI) and linear time periodic (LTP) frameworks [18] are briefly discussed to highlight the advantages and disadvantages of the NTD-PLL. Let us assume the TD-QSG signal $v_\alpha(t)$ as an undistorted grid voltage $v_g(t)$

$$v_\alpha\ (t) = v_g\,(t) = V_m \cos\left(\omega_g t - \phi\right) = V_m\ \cos\left(\theta_g\right) \tag{1}$$

where V_m, $\theta_g = \int \omega_g dt = \omega_n t + \int \Delta\omega_g dt$, and ϕ are the amplitude, phase angle, and initial phase angle of the grid voltage, respectively. The angular grid frequency $\omega_g = \omega_n + \Delta\omega_g$, where $\omega_n = 2\pi/T_s$ is the nominal angular grid frequency and $\Delta\omega_g$ is the angular grid frequency deviation from its nominal value. Delaying (1) by $T_s/4$ delay as discussed in [8] and [15] gives quadrature signal $v_\beta(t)$, expressed as

$$v_\beta\,(t) = v_\alpha\,(t - T_s/4) = V_m\ \sin\left(\theta_g - \Delta\omega_g T_s/4\right). \tag{2}$$

It is clear from (2) that v_α and v_β are orthogonal only for $\Delta\omega_g = 0$. From Fig. 2, the Park transformation (PT) matrix for NTD-PLL can be expressed as

$$R_{\mathrm{PT}}(\hat{\theta}) = \begin{bmatrix} \cos(\hat{\theta}) & \sin(\hat{\theta} - \Delta\hat{\omega}(T_s/4)) \\ -\sin\left(\hat{\theta} - \Delta\hat{\omega}\,(T_s/4)\right) & \cos\left(\hat{\theta}\right) \end{bmatrix} \tag{3}$$

where $\hat{\theta} = \int \hat{\omega} dt = \omega_n t + \int \Delta\hat{\omega} dt$ and $\hat{\omega} = \omega_n + \Delta\hat{\omega}$. The term $\Delta\hat{\omega}$ denotes estimation of frequency deviation from ω_n. Using (1)–(3) in $\left[v_d(t) \quad v_q(t)\right]^{\mathrm{T}} = R_{\mathrm{PT}}\,(\hat{\theta})[v_\alpha(t) \quad v_\beta(t)]^{\mathrm{T}}$ and solving for $v_q(t)$ signal gives

$$\begin{aligned} v_q(t) = (V_m/2)\Big[&\sin\left(\theta_g - \hat{\theta} + \Delta\hat{\omega}\,(T_s/4)\right) \\ &\underbrace{-\sin(\theta_g + \hat{\theta} - \Delta\hat{\omega}(T_s/4)) + \sin(\theta_g + \hat{\theta} - \Delta\omega_g\,(T_s/4))}_{D(t)} \\ &+\ \sin(\theta_g - \Delta\omega_g\,(T_s/4) - \hat{\theta})\Big]. \end{aligned} \tag{4}$$

Under a quasi-locked state, i.e., $\Delta\hat{\omega} \approx \Delta\omega_g$, the double-frequency oscillatory term $D(t) \approx 0$. Thus, (4) is rewritten as

$$\begin{aligned} v_q\,(t) \approx\ (V_m/2)\Big[&\Delta\theta_g - (\Delta\hat{\theta} - \Delta\hat{\omega}\,(T_s/4)) \\ &+ (\Delta\theta_g - \Delta\omega_g\,(T_s/4)) - \Delta\hat{\theta}\Big] \end{aligned} \tag{5}$$

where $\Delta\,\theta_g = \int \Delta\omega_g dt = \Delta\omega_g t$ and $\Delta\,\hat{\theta} = \int \Delta\hat{\omega} dt = \Delta\hat{\omega} t$. Applying the Laplace second shifting theorem [4], [7] to (5) yields

$$v_q\,(s) \approx V_m \underbrace{((1 + e^{-s(T_s/4)})/2)}_{dq\mathrm{DSC}_4(s)} \left[\Delta\theta_g\,(s) - \Delta\hat{\theta}\,(s)\right]. \tag{6}$$

The $dq\mathrm{DSC}_4(s)$ is a dq-frame delayed signal cancellation (dqDSC) operator with a delay factor of "4" [15]. From (6), the small-signal model (SSM) or LTI model of the suggested NTD-PLL is exemplified in Fig. 3. Thus, an open-loop transfer function $G_{\mathrm{ol}}(s)$ of NTD-PLL is expressed as

$$G_{\mathrm{ol}}\,(s) = ((1 + e^{-s(T_s/4)})/2)(k_p + (k_i/s))\,(V_m/s). \tag{7}$$

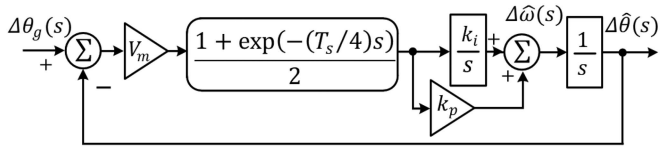

Fig. 3. LTI model of NTD-PLL.

Contrary to NTD-PLL in [4] and [10], it is interesting to note from (6) and Fig. 3 that, even during $\Delta\omega_g \neq 0$, the frequency $\hat{\omega}$ and phase estimation $\hat{\theta}$ from the suggested NTD-PLL are free from offset errors and DFOEs ($\because D(s) = 0$). The LTP model of the NTD-PLL is shown in Fig. 4 to assess the behavior of

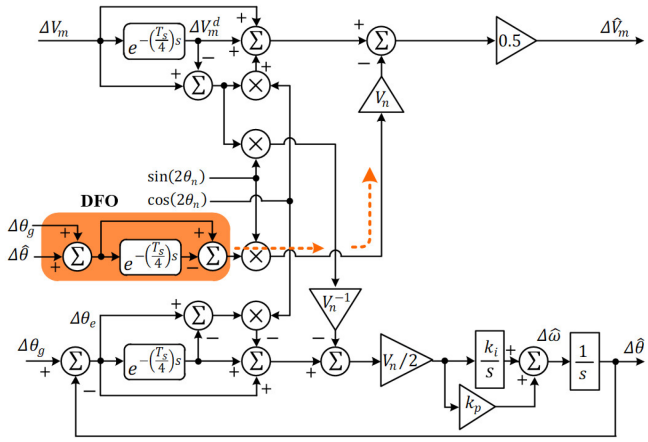

Fig. 4. LTP model of NTD-PLL [19].

the amplitude estimation $\hat{V}_m$. For the detailed LTP modeling approach and steps, the work in [15] and [18] can be referred. The additional oscillatory term, i.e., $(\Delta\theta_g + \Delta\hat{\theta}) - (\Delta\theta_g^d + \Delta\hat{\theta}^d)$ [15], [19] in Fig. 4, which is responsible for the DFOEs, is only coupled with v_d. Consequently, only $\hat{V}_m$ estimation suffers from DFOEs, whereas $\widehat{\omega}$ and $\hat{\theta}$ estimation are free from DFOEs during frequency jump. Therefore, a detailed analysis of the dynamic behavior of $\hat{V}_m$ is carried out in Sections III and IV to make the NTD-PLL structure a suitable choice for control, monitoring, and protection application in GCI under frequency deviations.

III. AEs Design for NTD-PLL

A. First Design Approach Using dq-Frame Component v_d

The structure of NTD-PLL in Fig. 2 is considered. The DFOEs in all single-phase QSG-based PLLs are attributed either due to nonorthogonality or due to the different amplitude of fundamental components, i.e., α and β axes signal. It is well known that α and β axes signal of TD-based QSG always exhibits nonorthogonality under off-nominal frequencies. Therefore, the DFOEs can be removed by correcting the nonorthogonal impact on amplitude estimation. The dq-frame component v_d can mathematically explain the phenomenon of increased DFOEs in NTD-PLL amplitude estimation during frequency variations. Using (1)–(3) in $[v_d(t) \quad v_q(t)]^{\mathrm{T}} = R_{\mathrm{PT}}\ (\hat{\theta})\ [v_\alpha(t) \quad v_\beta(t)]^{\mathrm{T}}$ and solving for $v_d(t)$ gives

$$
\begin{aligned}
{}^{(\mathrm{NTD})}v_d\ (t) = (V_m/2)\ \Big[&\cos\left(\theta_g - \hat{\theta}\right) + \cos\left(\theta_g + \hat{\theta}\right) \\
&+ \cos\left(\theta_g - \Delta\omega_g\,(T_s/4) - \hat{\theta} + \Delta\widehat{\omega}\,(T_s/4)\right) \\
&-\cos\left(\theta_g - \Delta\omega_g\,(T_s/4) + \hat{\theta} - \Delta\widehat{\omega}\,(T_s/4)\right)\Big].
\end{aligned} \tag{8}
$$

Under a quasi-locked state [4], $\hat{\theta} \approx \theta_g$, $\Delta\widehat{\omega} \approx \Delta\omega_g$, (8) can be approximated as

$$
\begin{aligned}
{}^{(\mathrm{NTD})}v_d\,(t) \approx V_m/2\Big[&\overbrace{\cos\left(\Delta\theta_g - \Delta\hat{\theta}\right)}^{\approx 1} + \cos\left(2\hat{\theta}\right) \\
&+ \overbrace{\cos\left(\Delta\theta_g - \Delta\omega_g\,(T_s/4) - \Delta\hat{\theta} + \Delta\widehat{\omega}\,(T_s/4)\right)}^{\approx 1} \\
&-\cos\left(2\hat{\theta} - 2\Delta\widehat{\omega}\,(T_s/4)\right)\Big].
\end{aligned} \tag{9}
$$

Applying product-to-sum trigonometric identity to (9) yields

$$
{}^{(\mathrm{NTD})}v_d\,(t) \approx V_m \underbrace{\left[\mathbf{1} - \sin\left(\boldsymbol{\delta_o}\right)\sin(2\hat{\theta} - \boldsymbol{\delta_o})\right]}_{\text{oscillatory disturbance}} \tag{10}
$$

where $\delta_o = \Delta\widehat{\omega}(T_s/4)$. Using the same process and assumptions, the amplitude estimation ${}^{(\mathrm{TD})}v_d(t)$ obtained from TD-PLL can also be derived as

$$
{}^{(\mathrm{TD})}v_d\,(t) \approx V_m\left[1 - \sin\left(\delta_o/2\right)\sin\left(2\hat{\theta} - \delta_o/2\right)\right]. \tag{11}
$$

For a small δ_o, the sine function in (10) and (11) can be approximated as [10]

$$
\begin{aligned}
{}^{(\mathrm{NTD})}v_d\,(t) &\approx V_m(1 - \delta_o \sin(2\hat{\theta} - \delta_o)) \\
{}^{(\mathrm{TD})}v_d\,(t) &\approx V_m(1 - (\delta_o/2)\sin(2\hat{\theta} - \delta_o/2)).
\end{aligned} \tag{12}
$$

From (12), it is evident that for the same $\Delta\widehat{\omega} \neq 0$, the magnitude of DFOEs in ${}^{(\mathrm{NTD})}v_d$ is twice that of the ${}^{(\mathrm{TD})}v_d$. The accuracy of (10) and (11) to predict the double-frequency oscillatory behavior in amplitude estimation is evaluated under phase and frequency jump, the results of which are shown in Fig. 5. It can be observed that the derived expressions properly predict their amplitude estimation behavior. By dividing the oscillatory disturbance term (shown in bold) onto both sides of (10), an efficient amplitude estimation can be obtained for NTD-PLL as

$$
{}^{(\mathrm{DFI})}_{v_d}\hat{V}_m \approx \frac{{}^{(\mathrm{NTD})}v_d\,(t)}{1 - \sin\left(\Delta\widehat{\omega}T_s/4\right)\sin(2\hat{\theta} - \Delta\widehat{\omega}T_s/4)} \tag{13}
$$

where ${}^{(\mathrm{DFI})}_{v_d}\hat{V}_m$ denotes the double-frequency immune amplitude estimation using d-axis component ${}^{(\mathrm{NTD})}v_d$. The estimation structure is referred to as the DFI-AE$_1$, concisely called AE$_1$. The subscript 1 is used to discriminate it from the second strategy, which will be investigated and designed in the following section. The proposed AE$_1$ is shown in Fig. 6(a).

B. Second Design Approach Using Pythagorean Trigonometric Identity (PTI) in $\alpha\beta$-Frame

The TD-QSG of NTD-PLL in Fig. 2 is considered for developing another amplitude estimation strategy using PTI, i.e.,

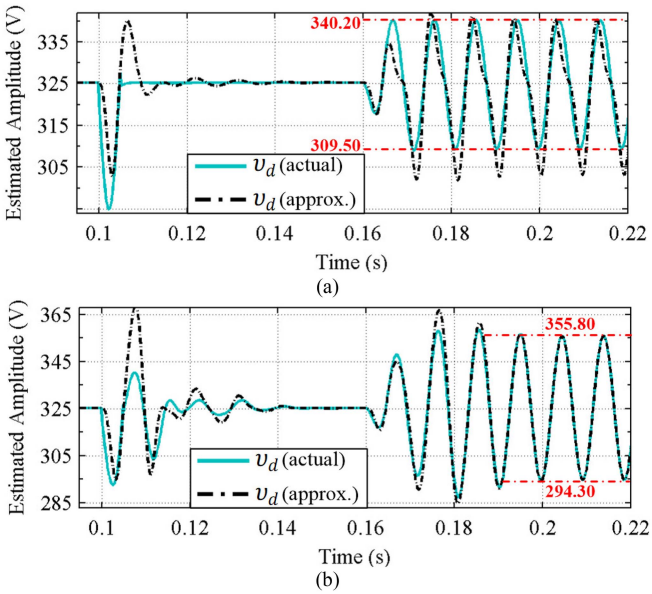

Fig. 5. Accuracy assessment of the amplitude estimation model. Parameters: $V_m = 230\sqrt{2}$ V, $\omega_n = 2\pi 50$, phase jump $= +10^\circ$ and frequency jump $= +3$ Hz at $t = 0.1$ and 0.16 s, respectively. Control parameters: $k_p = 325$ and $k_i = 24\,674$ for TD-PLL and $k_p = 166$ and $k_i = 11\,371$ for NTD-PLL. (a) TD-PLL. (b) NTD-PLL.

$\cos^2\theta + \sin^2\theta = 1$ in $\alpha\beta$-frame. Using (1) and (2) with $\Delta\omega_g = 0$, the expression $v_\alpha^2(t) + v_\beta^2(t)$ yields

$$v_\alpha^2(t) + v_\beta^2(t) = V_m^2\cos^2(\omega_g t) + V_m^2\sin^2(\omega_g t) = V_m^2. \tag{14}$$

Using (14), the amplitude can thus be estimated as

$$_{\text{PTI}}\hat{V}_m = \sqrt{v_\alpha^2(t) + v_\beta^2(t)} \tag{15}$$

where $_{\text{PTI}}\hat{V}_m$ denotes the amplitude estimation using the PTI approach. However, for $\Delta\omega_g \neq 0$, $v_\alpha^2(t) + v_\beta^2(t)$ yields

$$v_\alpha^2(t) + v_\beta^2(t) = V_m^2\cos^2(\omega_g t) + V_m^2\sin^2(\omega_g t - \delta_i) \tag{16}$$

while $\delta_i = \Delta\omega_g T_s/4$. Using double-angle formulae in (16) gives

$$v_\alpha^2(t) + v_\beta^2(t) = V_m^2\left[\frac{1+\cos(2\omega_g t)}{2} + \frac{1-\cos(2\omega_g t - 2\delta_i)}{2}\right]. \tag{17}$$

Applying product-to-sum trigonometric identity in (17) yields

$$v_\alpha^2(t) + v_\beta^2(t) = V_m^2\underbrace{[1 - \sin(\delta_i)\sin(2\omega_g t - \delta_i)]}_{\text{double-frequency oscillations}}. \tag{18}$$

It is worth noticing that for $\Delta\omega_g \neq 0$ the nonorthogonality between v_α and v_β results in DFOEs. The perfect elimination of the aforementioned undesired DFOEs present in (18) can be easily achieved for an efficient amplitude estimation as

$$_{\text{PTI}}^{(\text{DFI})}\hat{V}_m = \sqrt{\frac{v_\alpha^2(t) + v_\beta^2(t)}{1 - \sin(\Delta\omega_g T_s/4)\sin(2\omega_g t - \Delta\omega_g T_s/4)}} \tag{19}$$

where $_{\text{PTI}}^{(\text{DFI})}\hat{V}_m$ denotes the DFI amplitude estimation using the PTI approach. It can be observed that no approximation is made in $_{\text{PTI}}^{(\text{DFI})}\hat{V}_m$ as compared to $_{v_d}^{(\text{DFI})}\hat{V}_m$ in (13). Furthermore, since the $\hat{\theta} \approx \theta_g$, $\Delta\widehat{\omega} \approx \Delta\omega_g$, under quasi-locked state of NTD-PLL, the $\Delta\widehat{\omega}$ and $\hat{\theta}$ can be used for realizing (19). This amplitude estimation structure is referred to as DFI-AE$_2$, briefly called AE$_2$. The structure of the proposed AE$_2$ is shown in Fig. 6(b). It is worth appreciating from Fig. 6(b) (15) (19) that AE$_2$ requires a set of quadrature signals from the TD-QSG in $\alpha\beta$-frame and output signals from the PLL for accurately estimating the grid voltage amplitude under frequency variations. Therefore, AE$_2$ can be regarded as a generalized structure and can be used with other advanced TD-based PLLs.

C. Equivalence of $^{(TD)}v_d$ and Amplitude Estimated by PTI Unit

Using (18) in (15), expanding it using Newton's generalized binomial theorem and neglecting second and higher order terms [20] yield

$$\begin{aligned} _{\text{PTI}}\hat{V}_m &\approx V_m\left(1 - 0.5\sin(\delta)\sin(2\omega_g t - \delta)\right) \\ &\approx V_m\left(1 - \sin(\delta/2)\sin(2\omega_g t - \delta)\right) \end{aligned} \tag{20}$$

or equivalently, $_{\text{PTI}}\hat{V}_m \cong {}^{(\text{TD})}v_d$. It implies from (20) that the amplitude estimated using the PTI strategy is approximately equivalent to the $^{(\text{TD})}v_d$ obtained from TD-PLL.

IV. Enhancement of AE Structures

Although the proposed AE$_1$ and AE$_2$ eliminate the DFOEs from the amplitude estimation, it suffers from the following practical shortcomings.

1) Inability to provide a better estimate of the amplitude under harmonically distorted or noisy grid voltage signal.
2) It is now clear from (13) and (19) that a division operator is required for error-free estimation of the amplitude thus imposing real-time implementation complexity.

To overcome both issues, the AE structures are modified by using a low-pass filter (LPF) and a designer may avoid the division operator from the AE$_1$ and AE$_2$ structures [21]. To that end, the expression of AE$_1$ in (10) can be rewritten as

$$^{(\text{NTD})}v_d(t) = V_m - V_m\sin(\delta_o)\sin\left(2\hat{\theta} - \delta_o\right). \tag{21}$$

The first term on the right-hand side of (21) is the dc component V_m, which is the actual amplitude of the grid voltage, whereas the amplitude of double-frequency components depends on two terms. V_m and $\sin(\delta_o)$. Adding, double-frequency signal with the same amplitude into $^{(\text{NTD})}v_d(t)$ signal is suggested in this article for the complete cancellation of undesired double-frequency components and obtaining an error-free estimation of the fundamental amplitude. Therefore, a first-order LPF, with a cutoff frequency ω_p, may be considered in the proposed AEs as shown in Fig. 7.

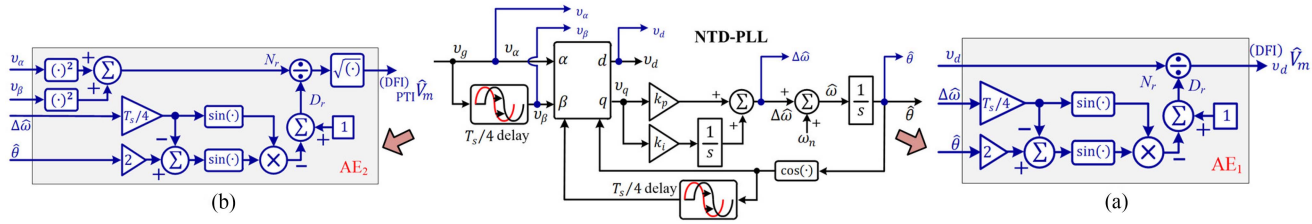

Fig. 6. AEs for NTD-PLL. (a) AE_1 utilizing $\boldsymbol{v_d}$. (b) AE_2 utilizing PTI.

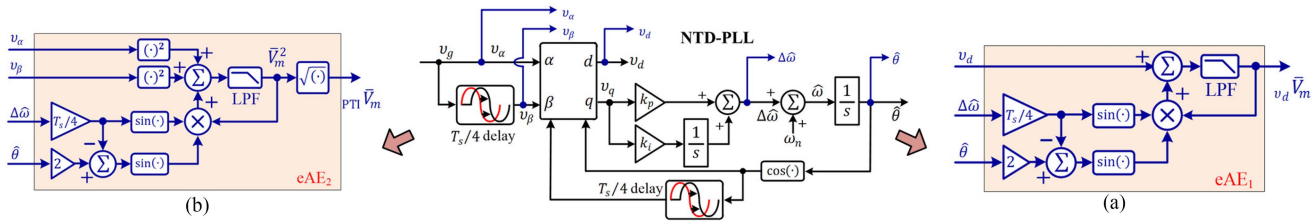

Fig. 7. Structure of eAEs for NTD-PLL. (a) DFI-eAE_1 utilizing v_d. (b) DFI-eAE_2 utilizing PTI.

A. AEs With LPF for Improved Filtering Capabilities

From Fig. 7(a) and (21), the amplitude estimation $\bar{V}_m$ can be expressed in the Laplace domain as

$$\bar{V}_m\ (s) = \frac{\omega_p}{s+\omega_p} \times \ell[^{(\mathrm{NTD})}v_d\,(t) + \bar{V}_m\,(t)\sin(2\hat{\theta}-\delta_o)\sin\,(\delta_o)] \tag{22}$$

where ℓ denotes the Laplace operator and LPF $(s) = \omega_p/(s+\omega_p)$. Multiplying both sides of (22) by $(s+\omega_p)$, transforming into the time domain, and rearranging them, gives

$$\dot{\bar{V}}_m\,(t) = \omega_p(\sin(2\hat{\theta}-\delta_o)\sin(\delta_o)-1)\bar{V}_m(t) + \omega_p{}^{(\mathrm{NTD})}v_d\,(t)\,. \tag{23}$$

Substituting (21) into (23) yields

$$\dot{\bar{V}}_m\,(t) = \omega_p(\sin(2\hat{\theta}-\delta_o)\sin(\delta_o)-1)\times\left\{\bar{V}_m\,(t)-V_m\right\}. \tag{24}$$

Considering the procedure presented in [21], where the two inputs and two outputs system is analyzed, a similar analysis may be carried out with single-input and single-output system. Assuming $\omega \cong \widehat{\omega}$ and input $[V_m]$ as a step function, a general time-domain expression for $\bar{V}_m(t)$ can be obtained as

$$\bar{V}_m\ (t) = V_m + H_1\,(\omega_f t)\,e^{-\omega_p t} \tag{25}$$

where $\omega_f = (\omega^2-\omega_p^2)^{0.5}$ and $H_1(\omega_f t)$ being the oscillatory term. Note that the detailed solution of (24) is not shown in the article to keep the discussion concise and clear. The designer may overlook the term $H_1(\omega_f t)$ as this fluctuating term will eventually decay to zero yielding an insignificant impact on the stability of the current proposal.

The aforementioned approach is also applied to the AE_2 for enhancing its performance. Using (18) and Fig. 7(b), $\bar{V}_m^2$ can be expressed in the Laplace domain in (26) as

$$\bar{V}_m^2\ (s) = \frac{\omega_p}{s+\omega_p} \times \ell\left[v_\alpha^2\,(t)+v_\beta^2\,(t) + \bar{V}_m^2\,(t)\sin\left(2\hat{\theta}-\delta_o\right)\sin\,(\delta_o)\right]. \tag{26}$$

Assuming $\omega \cong \widehat{\omega}$ and input $[V_m^2]$ as a step function, the expression for $\bar{V}_m^2(t)$ can be obtained as

$$\bar{V}_m^2\ (t) = V_m^2\ + H_2\,(\omega_f t)\,e^{-\omega_p t} \tag{27}$$

where $H_2(\omega_f t)$ is the oscillatory term. Taking square root on both sides, expanding (27) using Newton's binomial theorem and neglecting second and higher order terms [20] yields

$$\bar{V}_m\,(t) \cong V_m + (1/2)\,H_2\,(\omega_f t)\,e^{-\omega_p t}. \tag{28}$$

It is clear from (25) and (28) that the fluctuating terms $H_1(\omega_f t)$ and $H_2(\omega_f t)$ decay to zero with a time constant of $1/\omega_p$ and thereby enabling $\bar{V}_m(t)$ converge to V_m for accurate amplitude estimation. The effects are clearly illustrated in Fig. 8 corresponding to the structures as shown in Fig. 7. Among three different values of ω_p, ω_p= 500 rad/s enables the suggested AEs to achieve steady-state value within one fundamental cycle. As expected, the proposed method removes the DFOEs from the amplitude estimation, eliminates the use of the division operator, and capable of attaining better filtering capabilities. The structures are referred to as enhanced AE_1, briefly called eAE_1 [see Fig. 7(a)], and enhanced AE_2, briefly called eAE_2 [see Fig. 7(b)].

B. Approximated Implementation of AEs

As observed in Figs. 6 and 7, the complexity of computing two additional trigonometric functions should further be eased when low-cost implementation is a prime requirement. According to IEEE Standard 1159-2019 [22], the range of grid frequency

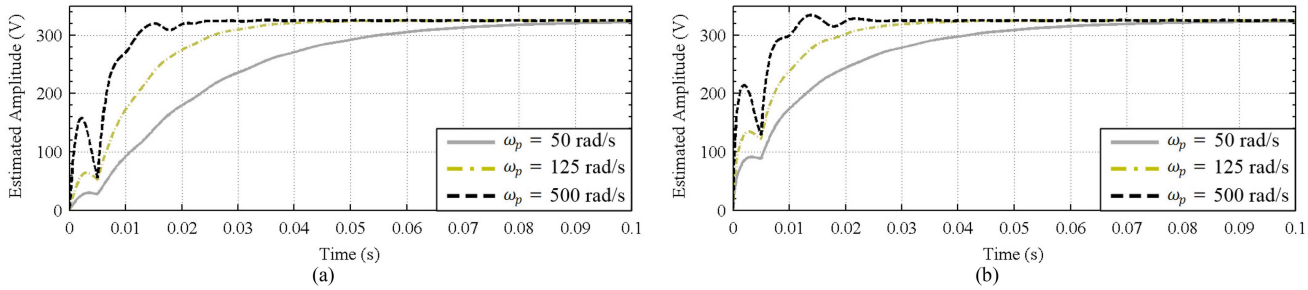

Fig. 8. Performance of eAEs under frequency deviation $= +5$ Hz at $t = 0$ s. (a) eAE_1. (b) eAE_2.

TABLE I
PERCENTAGE ERROR AND COMPUTATIONAL BURDEN IN APPROXIMATING TRIGONOMETRIC FUNCTION USING DIFFERENT METHODS

		Value at $\lvert\pm\pi/20\rvert$	Error (%)	Burden		
				T	+/−	×/÷
Actual	$\sin(\Delta\widehat{\omega}T_s/4)$	**0.156**434	**0**	1	0	0
Method 1 (M1)	$(\Delta\widehat{\omega}T_s/4) - (\Delta\widehat{\omega}T_s/4)^3/6$	**0.156**433	5.09e−4	0	3	1
Method 2 (M1)	$(\Delta\widehat{\omega}T_s/4)$	**0.157**079	0.4124	**0**	**0**	**0**

T = Trigonometric functions.

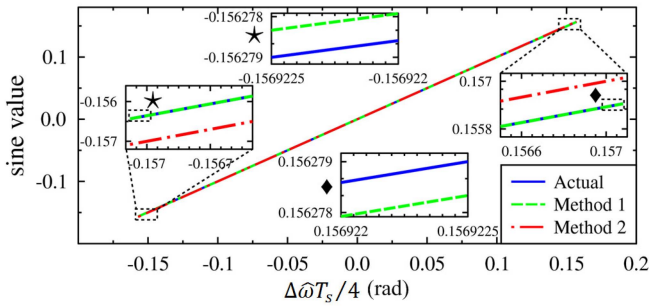

Fig. 9. Comparison of actual and approximated sine functions.

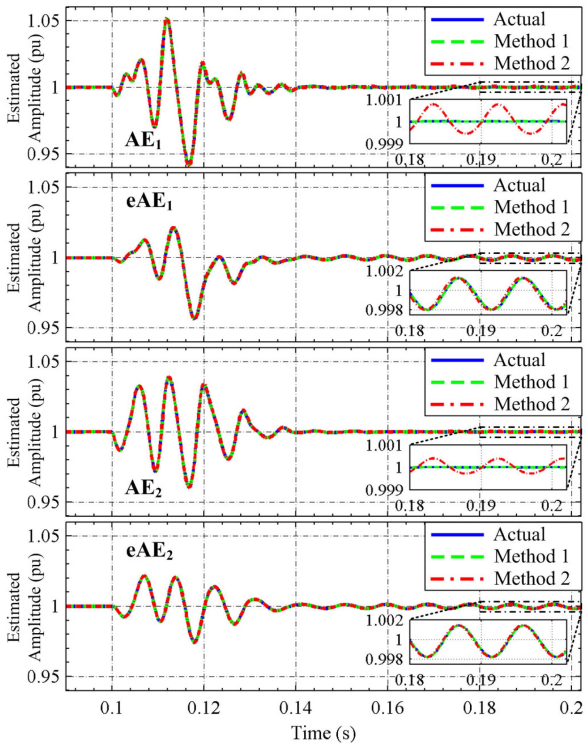

Fig. 10. Comparison of amplitude estimation between the actual and approximated structures of DFI-AEs under large (+5 Hz) frequency jump.

variation is 50 ± 0.10 Hz. However, for an exaggerated frequency deviation of 50 ± 5 Hz, i.e., $\Delta\widehat{\omega} = \pm 2\pi 5$ rad/s, the term $\Delta\widehat{\omega}T_s/4 = \pm\pi/20$ rad. For small phase angle $\Delta\widehat{\omega}T_s/4$, the trigonometric functions can be approximated by either of the following.

1) Method 1: Taylor's series expansion (neglecting third and higher terms).
2) Method 2: Small-angle approximation as presented in Table I.

This selection involves a tradeoff between the accuracy, range of maximum frequency deviation, and the computational burden for its optimized implementation. Fig. 9 compares the two approximations with the actual sine function, whereas the percentage error in approximating the sine function under a specified range is presented in Table I. Taylor's series expansion is more accurate but demands more computation, whereas the small-angle approximation exhibits the least computation with satisfactory accuracy. Furthermore, the comparison of the approximations with the original structure under the exaggeratedly large frequency jump (+5 Hz) is also shown in Fig. 10. The low-cost structure using method 2 shows very small ($\leq 0.02\%$) double-frequency oscillations as compared to the actual structure. In practice, the deviation will be much smaller, which further results in insignificant oscillations. Thus, the small-angle approximation is selected. The approximated structures of AEs are shown in Fig. 11. An in-depth complexity analysis in terms of execution time, and the number of operations required has been performed. The results are presented in Table II, where the best performances are highlighted in bold font. The proposed approximated AEs, thus allow for straightforwardly applying the NTD-PLL in a real-time practical application within the embedded microcontroller of the GCI without requiring additional computational power.

V. DESIGN CONSIDERATIONS AND NUMERICAL RESULTS

The SSMs of NTD-PLL with suggested AEs in Figs. 6 and 7 are the same as shown in Fig. 3 since the output of the AEs is not

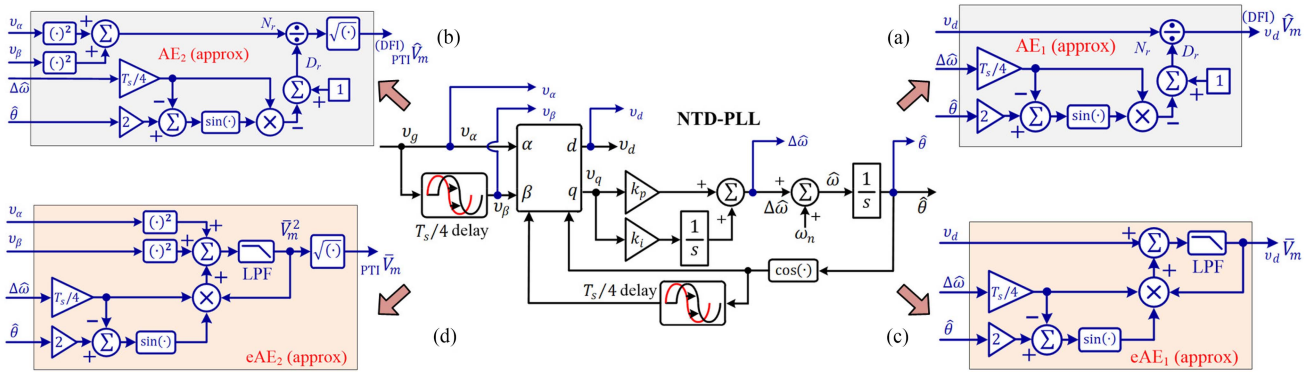

Fig. 11. Structure of approximated structures of AEs for NTD-PLL. (a) AE_1. (b) AE_2. (c) eAE_1. (d) eAE_2.

TABLE II
COMPLEXITY AND PERFORMANCE COMPARISON OF THE PROPOSED AEs FOR NTD-PLL

NTD-PLLs	#Complexity Comparison						Disturbance Rejection Capabilities in amplitude estimation			
	Operations					Execution time (μs)	Dynamic Response	DFDRC	HRC	NRC
	T	×	÷	√(·)	+/−					
AE_1	2	**5**	1	**0**	**3**	6.80	Medium	**Good**	Low	Low
AE_1 (approx.)	1	**5**	1	**0**	**3**	**6.05**	Medium	**Good**	Low	Low
AE_2	2	**5**	1	1	**3**	7.55	Medium	**Good**	Low	Low
AE_2 (approx.)	1	**5**	1	1	**3**	6.58	Medium	**Good**	Low	Low
eAE_1	2	7	**0**	**0**	6	11.30	**Good**	Medium	**Good**	**Good**
eAE_1 (approx.)	1	7	**0**	**0**	6	**9.60**	**Good**	Medium	**Good**	**Good**
eAE_2	2	7	**0**	1	6	12.35	**Good**	Medium	**Good**	**Good**
eAE_2 (approx.)	1	7	**0**	1	6	12.20	**Good**	Medium	**Good**	**Good**

T = Trigonometric functions. #AE_1 and eAE_1 include v_d, whereas AE_2 and eAE_2 include $v_\alpha^2 + v_\beta^2$ computation. All eAEs include LPF implementation.
DFDRC: Double-frequency disturbance rejection capabilities, **HRC**: Harmonic rejection capabilities, **NRC**: Noise rejection capabilities.

fed back to the control loop of the NTD-PLL. Thus, the AEs are not disturbing the loop structure of the NTD-PLL as expressed in (7). Therefore, the NTD-PLL control parameters can be fine-tuned using the existing methodologies like the symmetrical optimum (SO) [4], [7] or linear quadratic regulator (LQR) [17] method. Though, both the methods are well suited for the tuning of the control parameters, the LQR [17] is chosen over the SO method since the LQR approach analytically optimizes the control parameter without approximating the time-delay function of NTD-PLL, thereby achieving reduced control effort and better stability against disturbances. The LQR problem aimed to find the control input $u(t),\ t \in [0,\ \infty)$ that makes the following quadratic criterion J as small as possible [23], [24]:

$$J = \int_0^\infty \left(x^T(t)\,Qx(t) + u^T(t)\,Ru(t)\right)dt \tag{29}$$

where $Q\ (\geq 0) = Q^T$ and $R\ (>0) = R^T$ are a positive semidefinite and positive-definite weighting matrix, respectively, that penalizes the deviation of $x(t)$ and $u(t)$ from the equilibrium. For a linear process with time delay L, the optimal control solution $u(t)$ in (29) is defined [24] as

$$u(t) = \begin{cases} -R^{-1}B^T P e^{\left(A - BR^{-1}B^T P\right)t} e^{A(L-t)} x(t),\ 0 \leq t < L \\ -R^{-1}B^T P e^{\left(A - BR^{-1}B^T P\right)L} x(t),\ t \geq L \end{cases} \tag{30}$$

where $P > 0$ in (30) is a positive definite solution to algebraic Riccati equation [23], [24] given in (31) as

$$PA + A^T P - PBR^{-1}B^T P + Q = 0. \tag{31}$$

The PI controller for NTD-PLL is expressed as

$$\begin{aligned} u(t) &= \begin{bmatrix} k_i & k_p \end{bmatrix} \begin{bmatrix} \int e(t)\,dt & e(t) \end{bmatrix}^T \\ &= \begin{bmatrix} k_i & k_p \end{bmatrix} \begin{bmatrix} x_1(t) & x_2(t) \end{bmatrix}^T. \end{aligned} \tag{32}$$

The proportional and integral gains k_p and k_i can be determined by solving $u(t)$ in (30) and comparing with (32). An appropriate selection of Q and R weighting matrixes, that effects system performance and system input is required for solving (30). For simplicity, the element of Q matrix can be selected by appropriately choosing the value of ξ and ω_n [24]. When using ξ and ω_n for choosing Q matrix, J in (29) becomes $J \propto R$. This indicates that R is not contributing toward the design of the controller when tuning the NTD-PLL parameters. Therefore, we can always choose $R = 1$ (modified as scalar quantity), provided ξ and ω_n is used for Q matrix [23]. Here, $\xi = 0.3241$, $(T_s/4)\ \omega_n = 0.28$ rad/s are chosen without sacrificing the stability of the system [17]. The nominal grid frequency is kept fixed and set as 50 Hz, i.e., $\omega_n = 2\pi 50$ rad/s, thus, $T_s = 0.02$ s. The selected values of ξ and ω_n results in $k_p = 159$ and

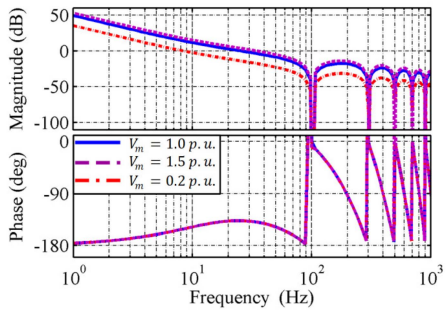

Fig. 12. Open-loop Bode plot of NTD-PLL with the proposed tuning parameters under sags and swells.

TABLE III
EMULATED GRID DISTURBANCES

Grid parameters	Symbols	Magnitude	Unit
Nominal grid voltage	v_g, V_m	230, 325.27	V (rms), V (peak)
Nominal grid frequency	f	50	Hz
Sampling frequency	f_s	10	kHz
Phase jump		10^o	
Sag		20	%
Frequency jump		+5	Hz
Swell		10	%
DC-offset		2	%
Noise (SNR)		17	dB
Harmonics#	$\|V_5\|$=6 %, $\|V_7\|$=5 %, $\|V_{11}\|$=3.5%, $\|V_{13}\|$=3%		

Maximum allowed values according to IEC standards (see [25] Table V).

k_i=11 360. For detailed design guidelines for tuning NTD-PLL using LQR, the work in [17] may be referred.

Fig. 12 shows the open-loop Bode plot of the NTD-PLL with AE using selected values of k_p and k_i. It can be observed that the phase margin (PM) of the NTD-PLL with AE is $\sim 43^\circ$. The tuning process assumes fixed grid voltage amplitude V_m. The stability analysis of the NTD-PLL with AE is also evaluated under voltage sag and swell as shown in Fig. 12 for different values of V_m. It can be observed that the PM is between 29° to 43° , which is within the range of PM for the stability of the control system [4]. The selection of cutoff frequency, ω_p for eAEs, however, involves tradeoffs between speed of response, overshoot and filtering capability. Here, ω_p= 500 rad/s is selected for satisfactory dynamic response and filtering capability.

Performance comparisons of NTD-PLL with AEs and eAEs were carried out through numerical studies under different grid disturbances. The parameters for numerical analysis are summarized in Table III. Fig. 13 shows the numerical results and Table II summarizes the disturbance rejection capabilities of the AEs.

A. Performance Under Grid Disturbances

Fig. 13(a) and (d) shows the performance under phase and frequency jump, respectively. The eAEs provide a better dynamic response than the AEs. The eAEs have 2% settling time, which is around one and a half cycles, whereas for AEs, it is around two cycles of the nominal frequency. The eAEs also offer a rather considerable decrease in the overshoot.

Fig. 13(b) illustrates the simulation results under the harmonic disturbances. It can be observed that both the AEs suffer from weak performance during distortion grid conditions. However, the eAEs show better harmonic rejection capability than the AEs. Fig. 13(c) shows the results when the input signal of NTD-PLL is contaminated with a zero-mean white Gaussian noise [10], [21]. It is observed that proposed eAEs have a better noise rejection capability compared to AEs due to the inclusion of LPF within the structure of eAEs.

B. Ride-Through Capability

The ride-through capability is another vital function for grid-connected power conditioning systems [26], [27], for which the implemented PLL needs to be synchronized with the grid voltage under severe voltage sag or swell. Voltage sag or swell is transitory [22], mainly caused by switching of large loads, energizing of transformers, and the connection of large induction motors. These are the most common power quality disturbances in the grid. The analysis of the proposed AE strategies in Sections III and IV assumes constant grid voltage amplitude. The efficacy of the proposed AEs is thus evaluated under a voltage sag of 0.8 p.u. and a swell of 0.5 p.u. during 0.02 and 0.06 s, respectively, as shown in Fig. 14. All the AEs are unaffected by severe grid voltage amplitude variations since fast estimation (within half to one cycle of the fundamental frequency) of the input voltage is achieved from the proposed AEs. It can be observed from Figs. 13 and 14 that compared to AEs, the eAEs exhibit better dynamic response and DRC under different grid disturbances but at the cost of speed of response.

VI. EXPERIMENTAL RESULTS

This section aims to evaluate the performance of NTD-PLL with proposed AEs under different grid disturbances through extensive experimental studies. To that end, a grid with a voltage signal $v_g\ (t) = V_m\ \cos(\omega_g t)$ is emulated using the dSPACE DS1104 hardware platform [13], [17], [28] and the grid is then superimposed with grid disturbances, having the parameters as presented in Table III [8], [12], [17], [21], [22], [23], [24], [25], [26], [27], [28]. The NTD-PLL with proposed AEs is prototyped on the dSPACE platform. The experimental setup is shown in Fig. 15. The parameters used in the numerical analysis were used for experimental evaluation. The ETD-PLL with parameters k_p = 440 and k_i = 48 361 [4] is also implemented to compare its amplitude estimation performance. Fig. 16 shows the experimental results of parameter estimates obtained using NTD-PLL. Throughout the result plots, each column represents different grid disturbances, and the first row of the subplots shows amplitude (V) using AE_1, AE_2, and eAE_2 and the grid voltage (V), whereas the second row of the subplots corresponds to frequency (Hz) and phase error ($^\circ$) estimations, along with amplitude estimation using eAE_1 and ETD-PLL, respectively.

It can be seen from Fig. 16(a) that the AEs reached steady state in about 25 ms (i.e., less than 1.5 cycles) and overshoot is limited to 4.6% during phase jump. From Fig. 16(b)–(d), the settling

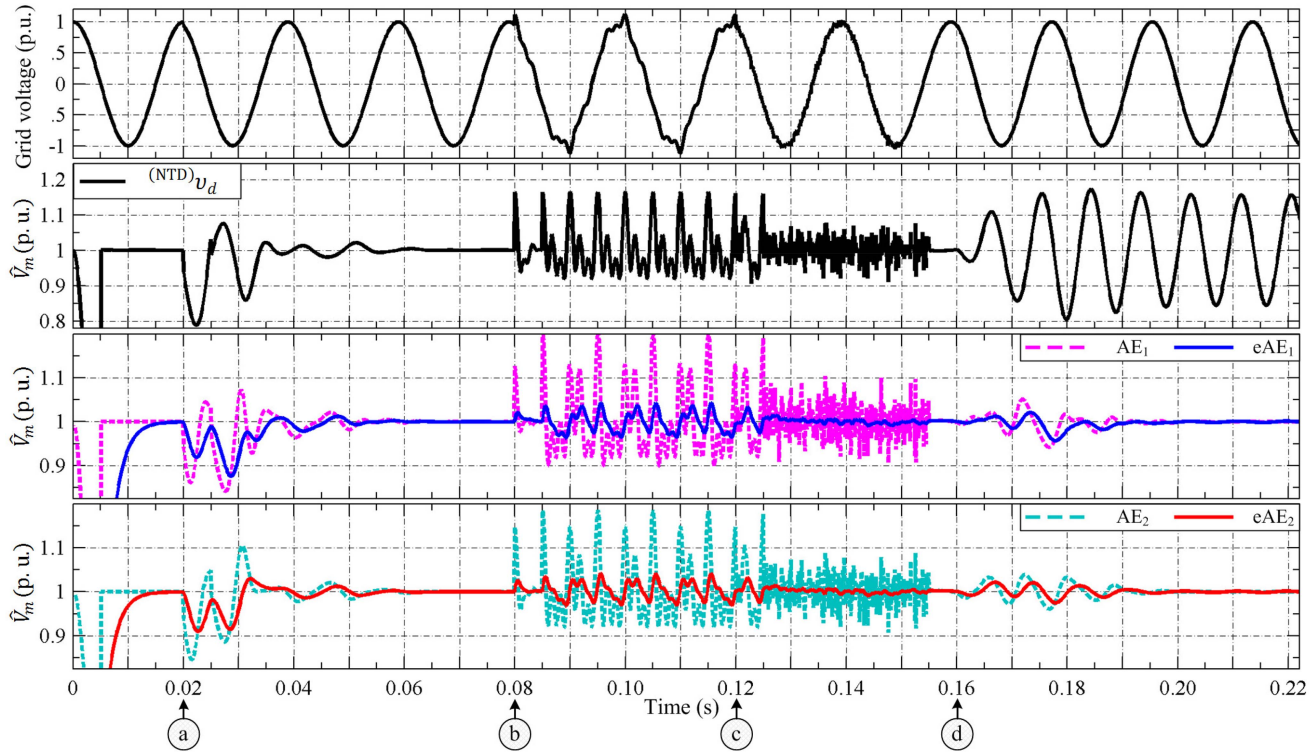

Fig. 13. Simulation results of the proposed AEs in response to (a) 20° phase jump, (b) harmonic distortion, (c) noise, and (d) +5 Hz frequency jump.

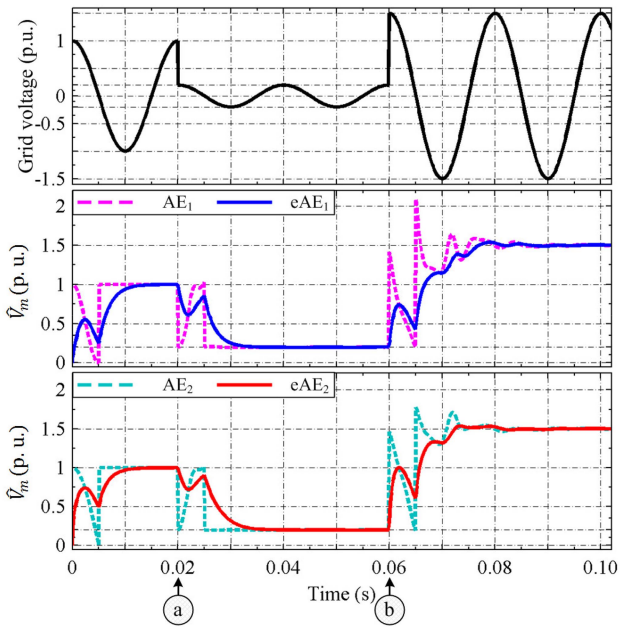

Fig. 14. Grid voltage waveform and estimated amplitude by suggested AEs under (a) 0.8 p.u. sag and (b) 0.5 p.u. swell.

time of AEs of NTD-PLL and ETD-PLL during sag and swell is around 15 ms (i.e., less than one cycle). However, contrary to ETD-PLL (with cascaded DSC operators), whose amplitude estimation waveform suffers from considerable steady-state oscillation as well as offset errors under the frequency deviation

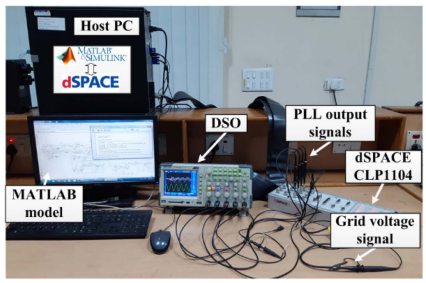

Fig. 15. Experimental setup.

[refer to Fig. 16(b)–(d)], the amplitude estimated by NTD-PLL using the proposed AEs is free from such errors and provides a steady estimation of the amplitude of the grid. The response of suggested AEs and ETD-PLL when adding a dc component to their input can be observed in Fig. 16(e). The transient behaviors of AEs and ETD-PLL have comparable oscillations since both the PLLs lack dc-offset disturbance rejection capabilities.

To highlight the advantages and disadvantages of the NTD-PLL with AEs, some existing PLLs, ATD-PLL, and frequency-fixed second-order generalized integrator PLL (FFSOGI-PLL) are also compared under the same test as presented in Table III. The parameters of these are set equal to the values suggested in [1], yielding almost the same bandwidth. The obtained results are summarized in Table IV. The maximum deviation, steady-state oscillation, steady-state deviation, and 2% settling time in AEs are denoted by ΔV_{pk}, ΔV_{ss}, ΔV_{errV}, and t_{ssV}, respectively. The two best performances are highlighted in bold font.

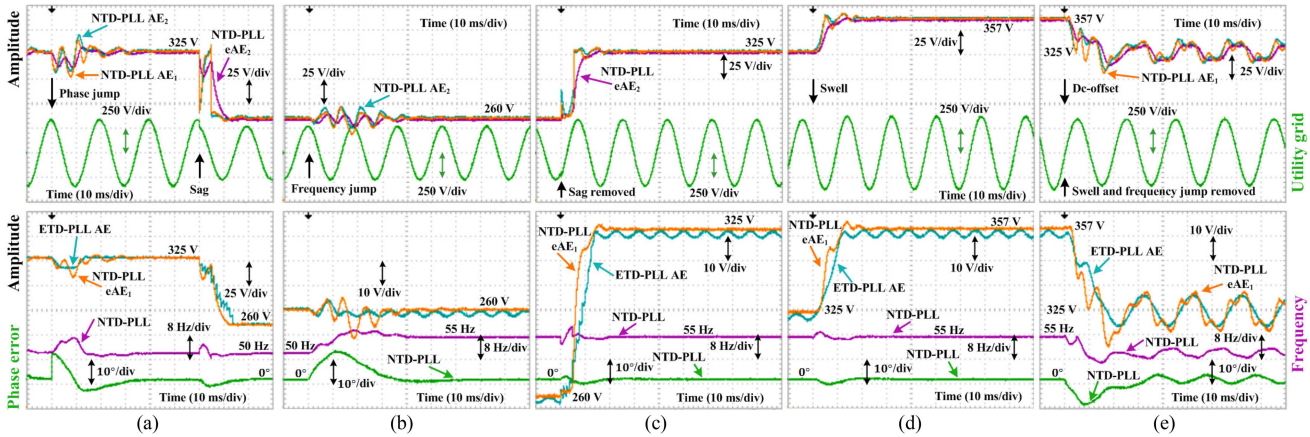

Fig. 16. Experimental results of the performance of NTD-PLL under grid disturbances. (a) Phase jump and sag. (b) Frequency jump. (c) Frequency jump with sag removed. (d) Frequency jump with a swell. (e) DC-offset with frequency jump and swell removed.

TABLE IV
PERFORMANCE COMPARISON OF AEs FROM VARIOUS PLLs

Disturbances	Parameters	ETD-PLL	ATD-PLL	VTD-PLL	FFSOGI-PLL	NTD-PLL AE_1	NTD-PLL AE_2	NTD-PLL eAE_1	NTD-PLL eAE_2
Phase jump	ΔV_{pk} (%)	**3.27**	7.55	8.90	8.34	**3.50**	4.70	5.87	4.54
	t_{ssV} (ms)	11.30	12.30	13.20	**10.30**	13.70	12.30	10.90	**10.40**
Harmonic	ΔV_{ss} (%)	**0.0**	25.60	23.98	**5.04**	32.11	27.76	8.24	6.73
Noise	ΔV_{ss} (%)	7.05	20.45	19.16	**1.87**	25.31	20.58	**5.85**	6.73
Sag	ΔV_{pk} (%)	0.0	24.86	24.98	0.0	27.37	25.75	**0.0**	**0.0**
	t_{ssV} (ms)	13.70	**5.00**	5.00	11.10	6.50	**5.00**	10.30	10.20
Swell	ΔV_{pk} (%)	**0.0**	7.90	7.45	**0.0**	8.81	8.18	6.18	5.18
	t_{ssV} (ms)	8.70	4.90	5.00	**3.80**	**5.00**	5.00	7.30	6.90
Frequency jump	ΔV_{pk} (%)	**0.0**	5.18	6.51	11.07	5.59	3.80	4.17	**2.45**
	ΔV_{ss} (%)	0.76	~ 0.0	~ 0.0	8.99	**0.0**	**0.0**	0.30	0.28
	t_{ssV} (ms)	0.0	44.70	44.50	0.0	26.40	**18.40**	20.40	**19.20**
	ΔV_{errV} (%)	0.72	~ 0.0	~ 0.0	5.41	**0.0**	**0.0**	~ 0.0	~ 0.0

From the obtained results, and Tables II and IV, the following suggestions can be made for selecting a particular AE for the specific applications.

1) AE_1 uses the dq-frame component of the PLL; therefore, AE_1 is PLL specific, whereas the AE_2 uses $\alpha\beta$-frame component of the TD-based PLLs, and thus AE_2 can be regarded as a generalized amplitude estimation strategy.
2) AE_1 and AE_2 are free from any DFOEs during frequency variation (refer to Fig. 10); however, they show slow dynamic response, poor noise immunity, and suffer from a weak performance under harmonic distortion. Therefore, we recommend using these AEs, where limited harmonics or noise, and large variations in frequency are expected in the grid and a rather slow dynamic response is not critical for the system.
3) To improve the dynamic performance and disturbance rejection capabilities, the AE_1 and AE_2 are introduced with an LPF and thereby eliminating the division operator.
4) The enhanced AEs, i.e., eAE_1 and eAE_2 have rather good noise immunity and harmonic disturbance rejection capability, though, a very small oscillation exists in amplitude estimation during the frequency variation (refer to Fig. 10). The observed oscillation can be further minimized by reducing the value of ω_p, but at the cost of slow transient response under various grid disturbances. Therefore, we recommend using these eAEs where large variations in harmonics and frequency variations are expected in the grid.
5) To reduce the implementation complexity, approximated structures of the AEs are also provided in Fig. 11.

VII. IMPACT OF NTD-PLL WITH THE PROPOSED AEs ON GCIs

Although the focus of this article is on adding the DFOEs rejection capability to AEs of NTD-PLL under frequency deviations and performance improvement under grid disturbances, the effectiveness of the proposed structure on the control of the GCIs is also explored under abnormal grid disturbances [29], [30]. To that end, the test system is shown in Fig. 17. The system parameters are provided in Table V. The current controller has been employed that also takes into account the $\hat{V}_m$. The controller has been tuned using the LQR approach [31], [32] where the tuning parameters are $k_1 = 790\,000$, $k_2 = 19\,000$, and $k_3 = 14.9$. The result obtained when a phase jump and a

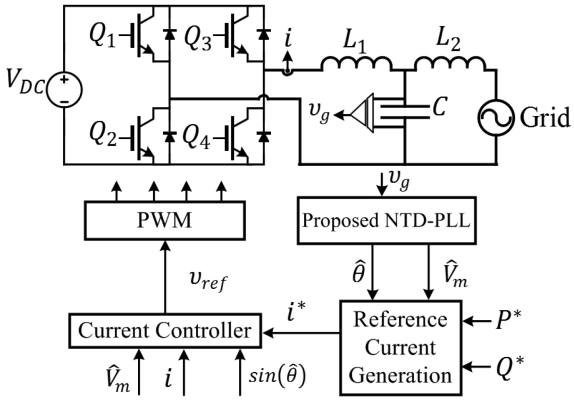

Fig. 17. Test system for a single-phase GCI system.

TABLE V
SINGLE-PHASE GCI PARAMETERS

Parameters	Symbols	Value	Unit
DC side voltage	V_{DC}	500	V
Inductance	L_1, L_2	5, 0.5	mH
Capacitance	C	10	μF
Switching frequency	f_{sw}	4	kHz
Active power rating	P_{rated}	2	kW
Reactive power rating	Q_{rated}	$\pm$2	kVAr
Current Limitations	$I_{max,min}$	$\pm$22	A

frequency jump are applied to the grid voltage is illustrated in Fig. 18.

The generation of unit template, i.e., $\sin(\hat{\theta})$ before the gate pulse is initiated before $t = 0.05$ s to ensure a soft-start of the GCI and soon after $t = 0.05$ s, the gate pulses are applied. At time $t = 0.1$ s, active power reference (P_{set}) command is set to 2 kW, which allows the GCI to inject the active power into the grid, whereas the reactive power reference (Q_{set}) command is set to 0 kVAr, as shown in Fig. 18(b). Note that the grid current reference, as well as the actual current, exhibits distorted waveform when NTD-PLL is implemented without AE structures, as exemplified in Fig. 18(a). The grid current reference, as well as actual current distortion, is significantly reduced when the proposed AE strategy is also employed with the NTD-PLL. It is important to stress that all the proposed approaches and the NTD-PLL are capable to handle the phase angle jump disturbance but the NTD-PLL alone fails to perform well under off-nominal frequency conditions. Also, the proposals eAE$_1$ and eAE$_2$ are less vulnerable to noise compared to the AE$_1$ and AE$_2$ approaches.

Furthermore, the performance of NTD-PLL on the control of GCI is also evaluated under grid voltage sag and swell conditions with different active and reactive power references. The result of the performances is shown in Figs. 19 and 20, respectively. It is obvious that a grid voltage sag invokes a faulty grid condition that requires a reactive power compensation but Q_{set} is 0 kVAr during $t = 0.2$–0.25 s, as shown in Fig. 19. Hence, an overshoot along with a higher amount of the inverter output current reaching an upper/lower bound (i.e., $I_{\max,\min} = \pm 22$ A)

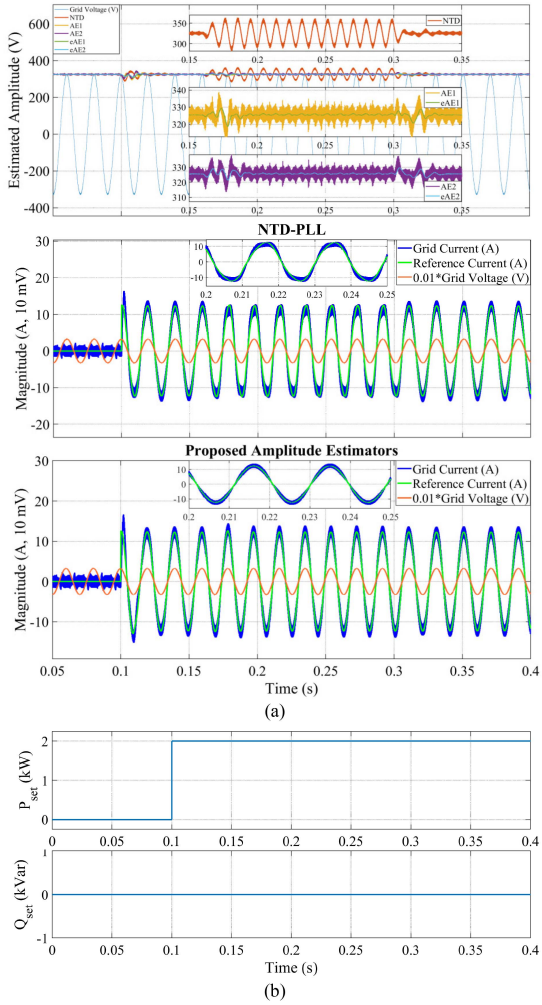

Fig. 18. Performance of GCI system following a 10° phase jump and +3 Hz frequency jump in the grid voltage at $t = 0.10$ and 0.16 s, respectively.

is observed to match the power balance between the GCI and the grid. Nevertheless, the current limiters are the rescuers, which help to limit the power converter being destabilized during this operation.

Therefore, the grid voltage sag tracking abilities can be easily verified, which indicates that the AE$_1$ and AE$_2$ possess similar dynamics, whereas eAE$_1$ and eAE$_2$ are slightly slower but can achieve better steady-state accuracy. In addition, the AE$_1$ and AE$_2$ suffer from steady-state oscillations as compared to the eAE$_1$ and eAE$_2$. Hence, the proposed AEs are well-suited for the low-voltage ride-through conditions.

Similarly, a test condition as explained in [32] is re-examined to warrant the potential abilities of the reactive power/current supply by the GCI to the grid but with a modified grid voltage condition, i.e., voltage swell, as exemplified in Fig. 20. Note that Q_{set} is set to +2 kVAr during $t = 0.15$–0.2 s, whereas P_{set} is already set at 2 kW; hence, GCI must supply a reactive current to the grid without reaching an upper/lower bound of $I_{\max,\min} = \pm 22$ A, ensuring a safe operation of the power converter with the grid while considering all the amplitude

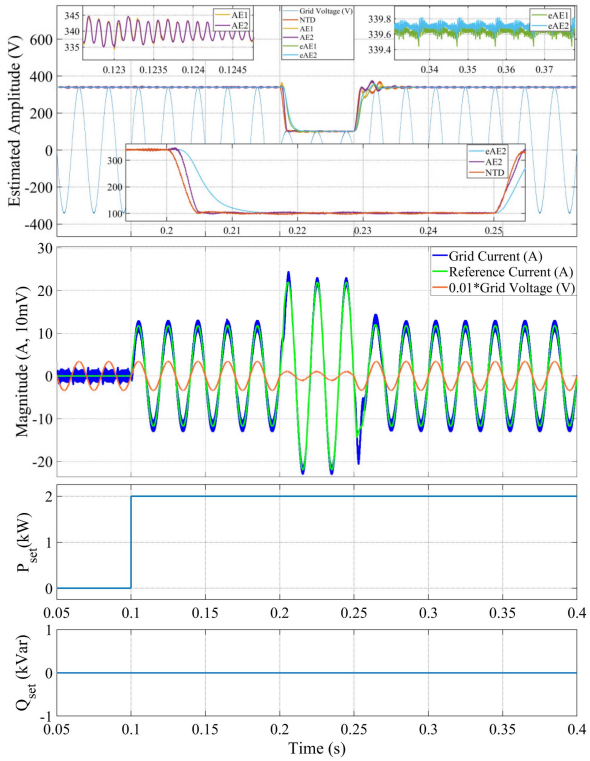

Fig. 19. Performance of GCI system following a 0.7 p.u. sag in the grid voltage from $t = 0.2$–0.25 s.

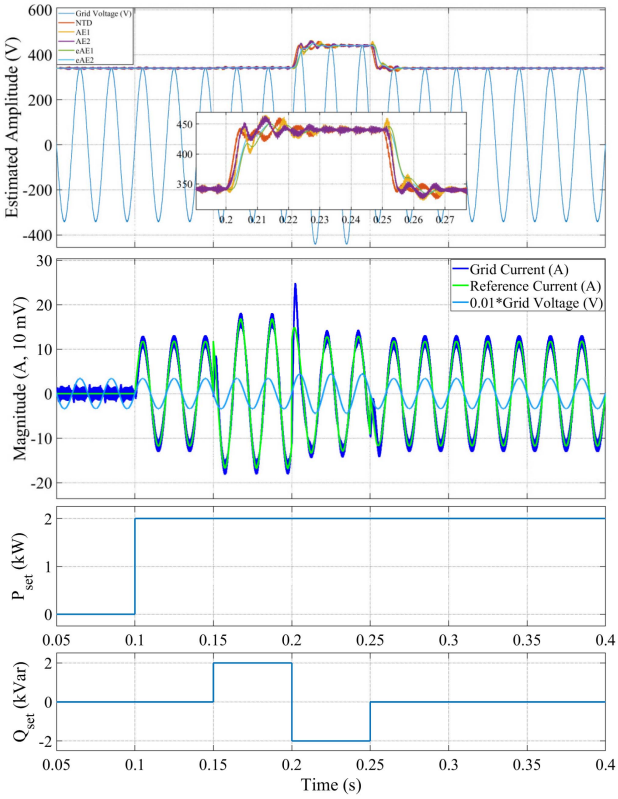

Fig. 20. Performance of GCI system following a 0.3 p.u. swell in the grid voltage from $t = 0.2$–0.25 s.

estimation approaches. However, a sharp rise in grid current is observed owing to the grid voltage swell, which requires reactive power compensation, i.e., Q_{set} is set at –2 kVAr during $t = 0.2$–0.25 s. A lagging current continues to flow toward the grid, whereas all the proposed estimators and the NTD-PLL ensure good tracking capability of the grid voltage swell. Hence, the proposed AEs ensure better tracking abilities and steady-state performance of the fundamental amplitude estimation under all the dynamic grid voltage conditions along with the off-nominal frequency excursions.

VIII. Conclusion

In this article, two approaches to eliminate the DFOEs in the amplitude estimation of NTD-PLL have been presented. One of the methods involves the d-axis signal, whereas the second approach employs PTI. Through a detailed mathematical analysis, it was established that the suggested methods effectively eliminate the undesired DFOEs from amplitude estimation. Strategies to enhance the dynamic performance and harmonic disturbance rejection capability of the proposed AEs were then explored. The performance of the NTD-PLL with proposed AEs was finally evaluated and compared against some well-known PLLs using numerical as well as experimental results. When examined for grid integration of GCI, the NTD-PLL with AE provides robust amplitude estimation along with minimal output power fluctuation.

References

[1] S. Golestan, J. M. Guerrero, and J. C. Vasquez, "Single-phase PLLs: A review of recent advances," *IEEE Trans. Power Electron.*, vol. 32, no. 12, pp. 9013–9030, Dec. 2017.

[2] J. Xu, H. Qian, S. Bian, Y. Hu, and S. Xie, "Comparative study of single-phase phase-locked loops for grid-connected inverters under non-ideal grid conditions," *CSEE J. Power Energy Syst.*, vol. 8, pp. 155–164, 2022.

[3] Y. Han, M. Luo, X. Zhao, J. M. Guerrero, and L. Xu, "Comparative performance evaluation of orthogonal-signal-generators-based single-phase PLL algorithms—A survey," *IEEE Trans. Power Electron.*, vol. 31, no. 5, pp. 3932–3944, May 2016.

[4] S. Golestan, J. M. Guerrero, A. Vidal, A. G. Yepes, J. Doval-Gandoy, and F. D. Freijedo, "Small-signal modeling, stability analysis and design optimization of single-phase delay-based PLLs," *IEEE Trans. Power Electron.*, vol. 31, no. 5, pp. 3517–3527, May 2016.

[5] M. Bertoluzzo, S. Giacomuzzi, and A. Kumar, "Design and experimentation of a single-phase PLL with novel OSG method," *IEEE Access*, vol. 10, pp. 33393–33407, 2022.

[6] L. Xiong, F. Zhuo, F. Wang, X. Liu, and M. Zhu, "A fast orthogonal signal-generation algorithm characterized by noise immunity and high accuracy for single-phase grid," *IEEE Trans. Power Electron.*, vol. 31, no. 3, pp. 1847–1851, Mar. 2016.

[7] S. Golestan, "Modeling, analyzing, and designing advanced synchronization techniques for power converters," Ph.D. dissertation, Faculty Eng. Sci., Aalborg Universitet, Aalborg, Denmark, 2018.

[8] M. A. Akhtar and S. Saha, "Analysis and comparative studies on impact of transport delay and transforms on the performance of TD-PLL for single phase GCI under grid disturbances," *Int. J. Elect. Power Energy Syst.*, vol. 115, 2020, Art. no. 105488.

[9] I. A. Smadi and B. H. B. Fawaz, "Phase-locked loop with DC offset removal for single-phase grid-connected converters," *Elect. Power Syst. Res.*, vol. 194, 2021, Art. no. 106980.

[10] S. Golestan, J. M. Guerrero, A. Abusorrah, M. M. Al-Hindawi, and Y. Al-Turki, "An adaptive quadrature signal generation-based single-phase phase-locked loop for grid-connected applications," *IEEE Trans. Ind. Electron.*, vol. 64, no. 4, pp. 2848–2854, Apr. 2017.

[11] K. Saleem, Z. Ali, and K. Mehran, "A single-phase synchronization technique for grid-connected energy storage system under faulty grid conditions," *IEEE Trans. Power Electron.*, vol. 36, no. 10, pp. 12019–12032, Oct. 2021.
[12] L. Hadjidemetriou, Y. Yang, E. Kyriakides, and F. Blaabjerg, "A synchronization scheme for single-phase grid-tied inverters under harmonic distortion and grid disturbances," *IEEE Trans. Power Electron.*, vol. 32, no. 4, pp. 2784–2793, Apr. 2017.
[13] S. Golestan, J. M. Guerrero, J. C. Vasquez, A. M. Abusorrah, and Y. Al-Turki, "Research on variable-length transfer delay and delayed-signal-cancellation-based PLLs," *IEEE Trans. Power Electron.*, vol. 33, no. 10, pp. 8388–8398, Oct. 2018.
[14] S. Gautam, Y. Lu, W. Hassan, W. Xiao, and D. D.-C. Lu, "Single phase NTD PLL for fast dynamic response and operational robustness under abnormal grid condition," *Elect. Power Syst. Res.*, vol. 180, Mar. 2020, Art. no. 106156.
[15] M. A. Akhtar, S. Saha, and R. Singh, "A second look on nonfrequency-dependent transport delay-based PLL: Performance enhancement under frequency deviations," *IEEE Trans. Power Electron.*, vol. 36, no. 12, pp. 13365–13371, Dec. 2021.
[16] S. Gautam, Y. Lu, W. Xiao, D. D.-C. Lu, and M. S. Golsorkhi, "Dual-loop control of transfer delay based PLL for fast dynamics in single-phase AC power systems," *IET Power Electron.*, vol. 12, pp. 3571–3581, 2019.
[17] M. A. Akhtar and S. Saha, "A systematic approach of loop filter tuning of TD-based PLLs using LQR-based approach considering time delay," *IEEE J. Emerg. Sel. Topics Power Electron.*, vol. 10, no. 2, pp. 2424–2434, Apr. 2022.
[18] S. Golestan, J. M. Guerrero, and J. C. Vasquez, "LTP modeling of single-phase T/4 delay-based PLLs," *IEEE Trans. Ind. Electron.*, vol. 68, no. 9, pp. 9003–9008, Sep. 2021.
[19] M. A. Akhtar and S. Saha, "A truly NTD-based PLL: Simple approach of double-frequency oscillation rejection," *IEEE Trans. Power Electron.*, vol. 37, no. 2, pp. 1217–1222, Feb. 2022.
[20] J. Morales and A. Flores-Riveros, "The generalization of the binomial theorem," *J. Math. Phys.*, vol. 30, no. 2, pp. 393–397, 1989.
[21] S. Golestan, M. Monfared, F. D. Freijedo, and J. M. Guerrero, "Design and tuning of a modified power-based PLL for single-phase grid-connected power conditioning systems," *IEEE Trans. Power Electron.*, vol. 27, no. 8, pp. 3639–3650, Aug. 2012.
[22] *IEEE Recommended Practice for Monitoring Electric Power Quality*, IEEE Standard 1159-2019 (Revision of IEEE Standard 1159-2009), pp. 1–98, 2019.
[23] J.-B. He, Q.-G. Wang, and T.-H. Lee, "PI/PID controller tuning via LQR approach," *Chem. Eng. Sci.*, vol. 55, pp. 2429–2439, Jul. 2000.
[24] D. Xue, Y. Chen, and D. Atherton, *Linear Feedback Control: Analysis and Design With MATLAB*. Philadelphia, PA, USA: SIAM, 2007.
[25] S. Golestan, M. Ramezani, J. M. Guerrero, and M. Monfared, "dq-Frame cascaded delayed signal cancellation-based PLL: Analysis, design, and comparison with moving average filter-based PLL," *IEEE Trans. Power Electron.*, vol. 30, no. 3, pp. 1618–1632, Mar. 2015.
[26] A. Sahoo, J. Ravishankar, M. Ciobotaru, and F. Blaabjerg, "Enhanced fault ride-through of power converters using hybrid grid synchronization," *IEEE J. Emerg. Sel. Topics Power Electron.*, vol. 10, no. 3, pp. 2829–2841, Jun. 2022.
[27] A. T. Nguyen and D.-C. Lee, "Advanced grid synchronization scheme based on dual eSOGI-FLL for grid-feeding converters," *IEEE Trans. Power Electron.*, vol. 37, no. 6, pp. 7218–7229, Jun. 2022.
[28] M. A. Akhtar and S. Saha, "An adaptive frequency-fixed second-order generalized integrator-quadrature signal generator using fractional-order conformal mapping based approach," *IEEE Trans. Power Electron.*, vol. 35, no. 6, pp. 5548–5552, Jun. 2020.
[29] A. Bamigbade and V. Khadkikar, "Parameter estimation and grid synchronization using a first-order frequency-locked loop," *IEEE Trans. Instrum. Meas.*, vol. 71, Jan. 2022, Art. no. 6500113.
[30] S. Gautam, Y. Lu, S. Taghizadeh, W. Xiao, and D. D.-C. Lu, "An enhanced time-delay-based reference current identification method for single-phase system," *IEEE J. Emerg. Sel. Topics Ind. Electron.*, vol. 3, no. 3, pp. 683–693, Jul. 2022.
[31] S. A. Khajehoddin, M. Karimi-Ghartemani, and M. Ebrahimi, "Optimal and systematic design of current controller for grid-connected inverters," *IEEE J. Emerg. Sel. Topics Power Electron.*, vol. 6, no. 2, pp. 812–824, Jun. 2018.
[32] M. Karimi-Ghartemani, H. Karimi, S. A. Khajehoddin, and S. M. Hoseinizadeh, "Efficient modeling and systematic design of enhanced phase-locked loop structures," *IEEE Trans. Power Electron.*, vol. 37, no. 8, pp. 9061–9072, Aug. 2022.

Mohd. Afroz Akhtar (Member, IEEE) was born in Varanasi, India, in 1987. He received the B.Tech. degree in electrical engineering from Jamia Millia Islamia, New Delhi, India, in 2010, and the M.Tech. degree in mechatronics engineering and Ph.D. degree in engineering sciences from Council of Scientific and Industrial Research–Central Mechanical Engineering Research Institute (CSIR-CMERI) Campus, Academy of Scientific and Innovative Research (AcSIR), Durgapur, India, in 2012 and 2020, respectively.

From 2010 to 2012, he was a Quick Hire Scientist (Trainee) with CSIR-CMERI, Durgapur, India, where since 2012, he has been a Scientist, and also as an Assistant Professor with the CSIR-CMERI Campus, AcSIR. His research interests include modeling and control of power converters in power, BLDC/PMSM/SRM motor drives applications, synchronization techniques, and electromagnetics.

Suman Saha was born in Durgapur, India, in 1977. He received the B.E. degree in electrical engineering from Jalpaiguri Government Engineering College, Jalpaiguri, India, in 2003, the M.E. degree in electrical engineering from Indian Institute of Engineering Science and Technology, Howrah, India, in 2007, and the Ph.D. degree in engineering sciences from Jadavpur University, Kolkata, India, in 2012.

He has been the Principal Scientist with the Council of Scientific and Industrial Research–Central Mechanical Engineering Research Institute (CSIR-CMERI), Durgapur, India, and also an Associate Professor with the CSIR-CMERI Campus, AcSIR. His research interests include vehicle dynamics and control of EV, e-motor drives, fractional-order system and control, and electromagnetic analysis of actuators.

Dibyendu Pal received the B.Tech. degree in electronics and communication engineering from Kalyani Government Engineering College, Kalyani, India, in 2002.

Since 2004, he has been a Scientist with the Council of Scientific and Industrial Research–Central Mechanical Engineering Research Institute, Durgapur, India. His research interests include system engineering, navigation and guidance and motion control, and process automation and control design using MATLAB/Simulink platform for robotic/underwater/industrial applications.

Anant Kumar Verma (Member, IEEE) received the bachelor's degree in instrumentation engineering from the University Science Instrumentation Center, Srinagar, India, in 2012, the master's degree in power electronics and drives from the Dehradun Institute of Technology, Dehradun, India, in 2014, and the Ph.D. degree in electrical engineering from the National Institute of Technology, Hamirpur, India, in 2021.

He is currently a Postdoctoral Researcher with the Institute of Engineering Sciences, Universidad de O'Higgins, Rancagua, Chile. His research interests include renewable energy systems, modeling of grid synchronization algorithms, battery energy storage systems, and control of power electronic converters.

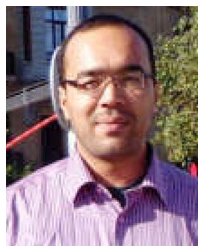

Zoheir Tir (Senior Member, IEEE) was born in El Oued, Algeria. He received the B.Sc. degree in electrical engineering from the University of Batna 2, Fesdis, Algeria, in 2007, the M.Sc. degree in electrical engineering from the University of Setif, Setif, Algeria, in 2010, and the Sc.D. degree in electrical engineering from the University of Batna 2, in 2014.

In December 2020, he was promoted to the rank of Professor in the field of electrical engineering with the University of El Oued, El Oued, Algeria, where he carried out research activities with the LEVRES Laboratory. His research project involves automatic control and its implementation on ac motor drives, renewable energy systems, observers, estimators, and DSP-based real-time control.